Supporting Information

Large-Area, Crosstalk-Free, Flexible Tactile Sensor Matrix Pixelated by Mesh Layer

Kyubin Bae[†], Jinho Jeong[†], Jongeun Choi[†], Soonjae Pyo[‡], and Jongbaeg Kim[†]**

[†] School of Mechanical Engineering, Yonsei University, 50 Yonsei-ro, Seodaemun-gu, Seoul, 03722, Republic of Korea

[‡] Department of Mechanical System Design Engineering, Seoul National University of Science and Technology, 232 Gongneung-ro, Nowon-gu, Seoul, 01811, Republic of Korea

Corresponding Author

Prof. Jongbaeg Kim*

School of Mechanical Engineering, Yonsei University

E-mail: kimjb@yonsei.ac.kr

Prof. Soonjae Pyo*

Department of Mechanical System Design Engineering, Seoul National University of Science and Technology

E-mail: sjpyo@seoultech.ac.kr

Contents

Figure S1. Detailed fabrication process of the mesh-embedded tactile sensor array.

Figure S2. Total area of fabricated sensor.

Figure S3. CNT exposure on the sensor surface after etching.

Figure S4. Detailed schematic of the experimental setup.

Figure S5. Uniformity of each cell of the fabricated sensor.

Figure S6. Changes in the current of the sensor before and after etching.

Figure S7. The change in current of the sensor according to applied force.

Figure S8. Sensor current change according to minute pressure.

Figure S9. Current value of adjacent cells according to pressure during crosstalk test.

Figure S10. The changes in current of the 9 cells of the mesh-based sensor and the conventional sensor.

Figure S11. Initial contact area between the sensing material and electrode in planar and bent state.

Figure S12. Various data point distributions and SVM classification examples.

Figure S13. Two cases when braille “N” is pressed.

Figure S14. Block diagram from current measurement to visualization system.

Table S1. Cross-validation prediction accuracy using ideal Braille data.

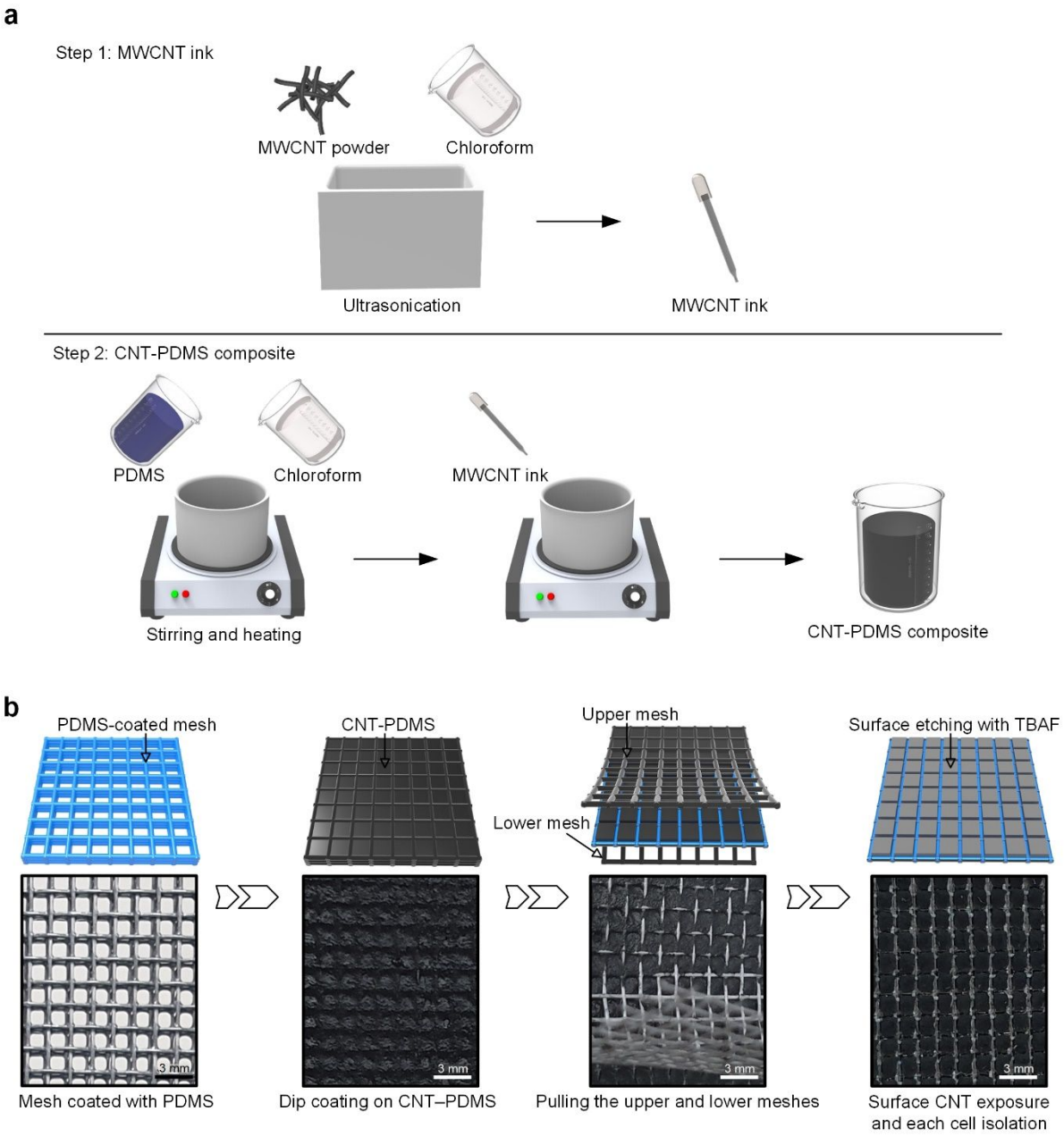

Figure S1. a) Fabrication process of the CNT–PDMS solution. b) Photographs corresponding to each process in the fabrication of the mesh-embedded composite

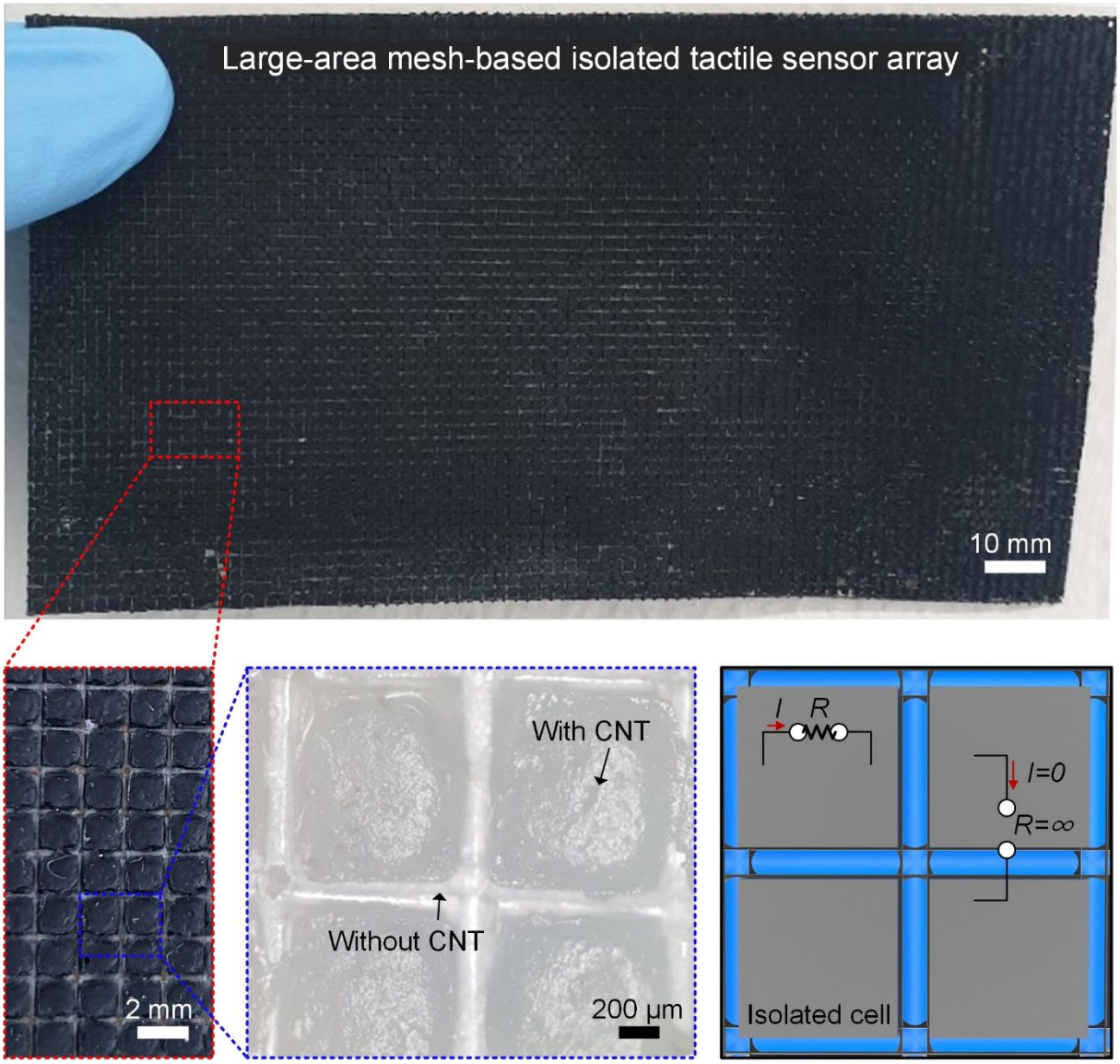

Figure S2. As-fabricated mesh-embedded composite (180 mm × 100 mm). The optical microscope and SEM images show that each composite is separated by the mesh.

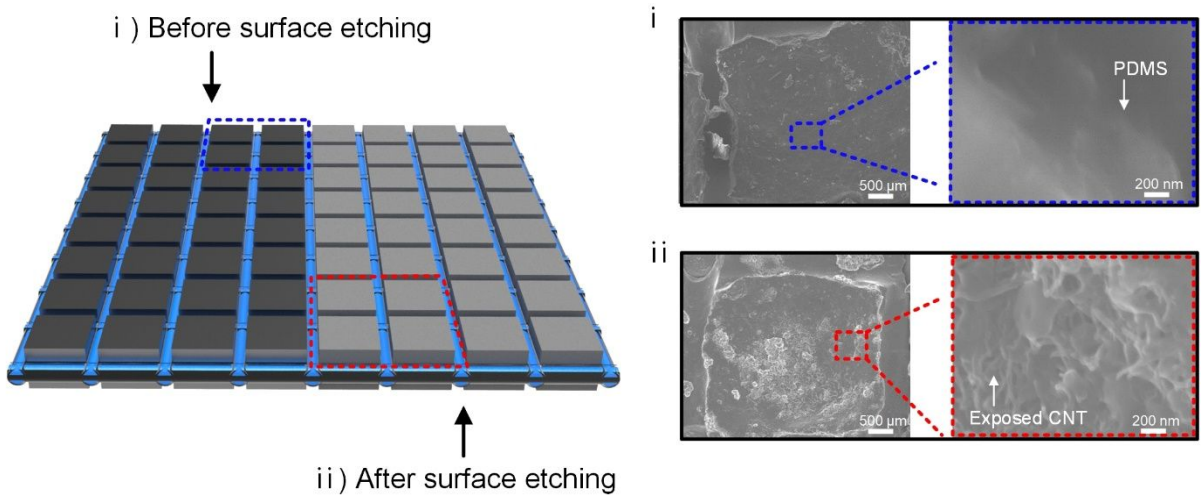

Figure S3. SEM images of the top surface of the composite ⅰ) before and ⅱ) after the etching process.

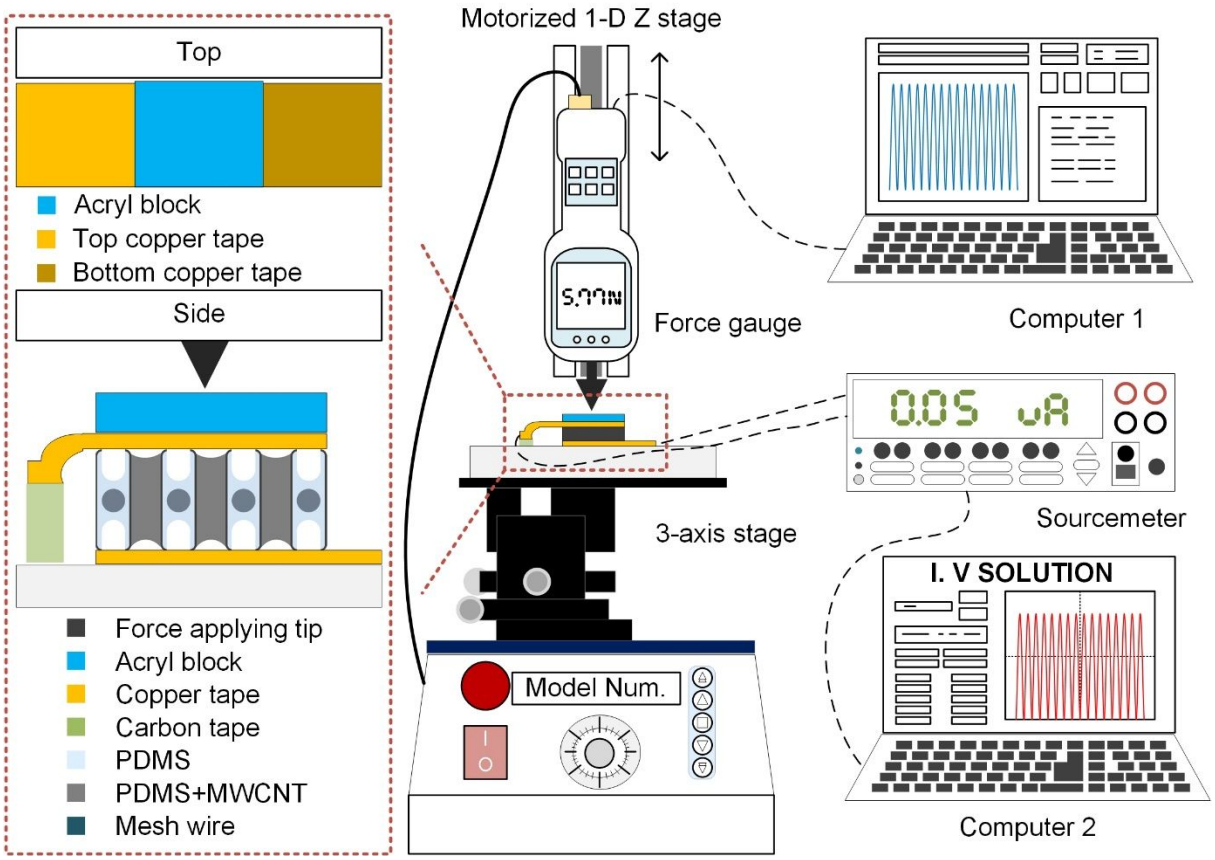

Figure S4. Detailed schematic of the experimental setup

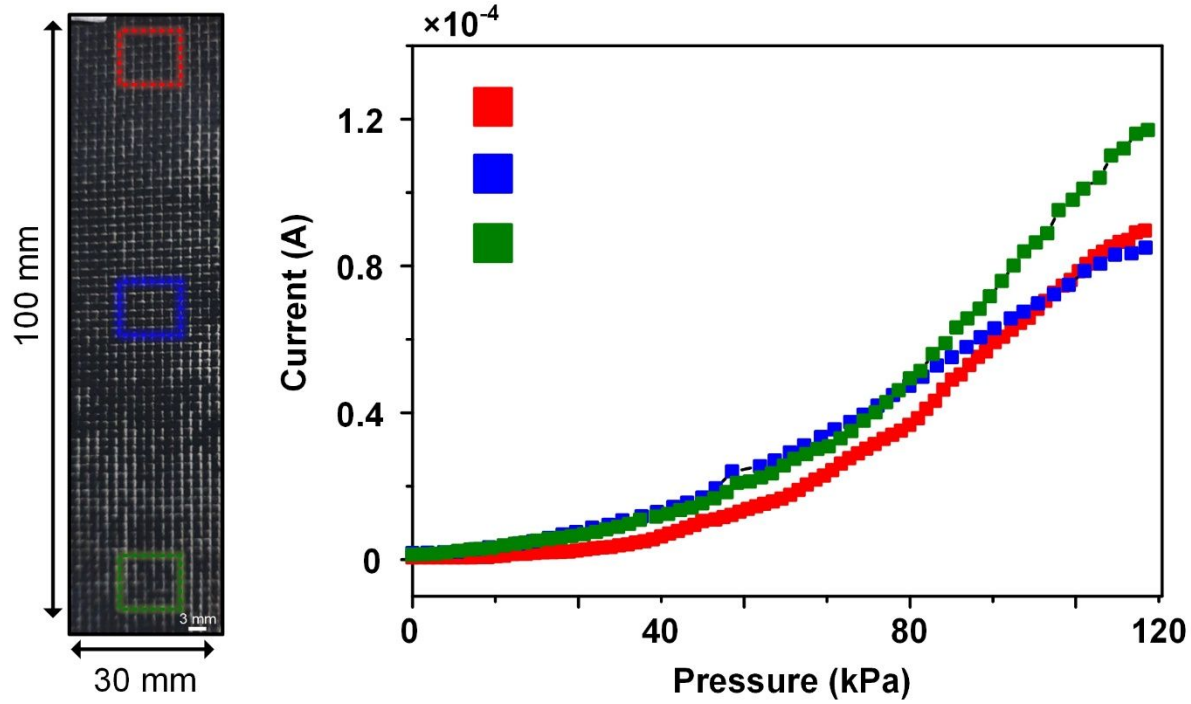

Figure S5. Dependence of the sensing performance on the position of the applied pressure. Although the sensing characteristics slightly vary according to the position, the deviation can be minimized by employing industrial-level equipment.

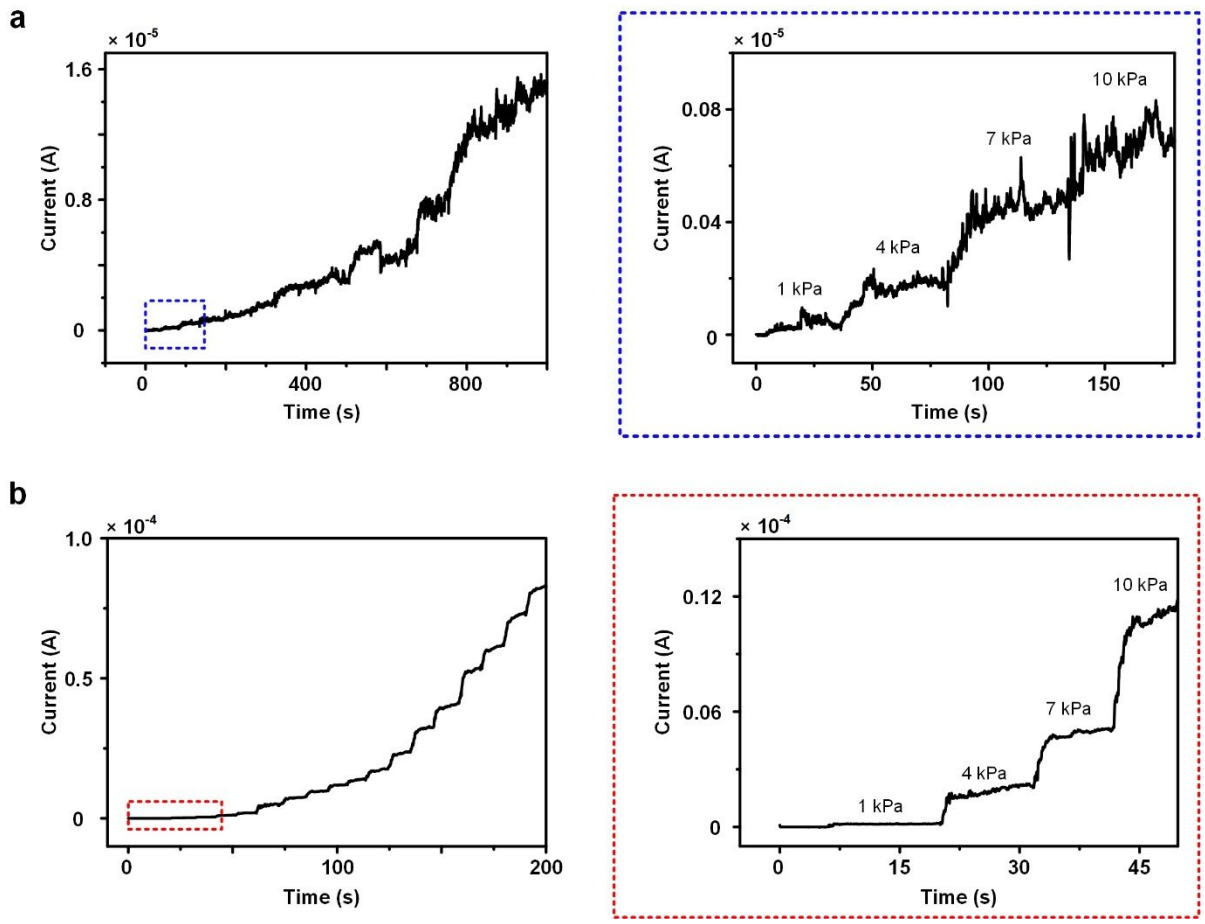

Figure S6. Changes in the current of the sensor with (a) the unetched and (b) etched composites with increasing pressure

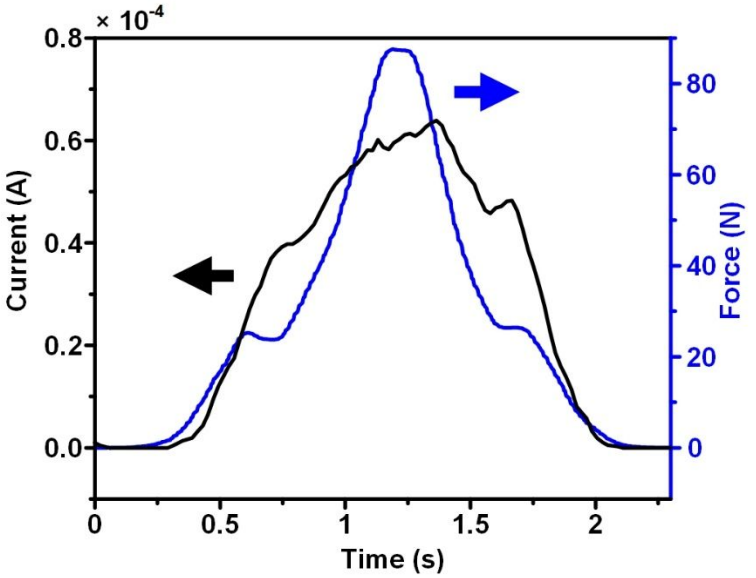

Figure S7. The change in current of the sensor according to increasing and decreasing applied force.

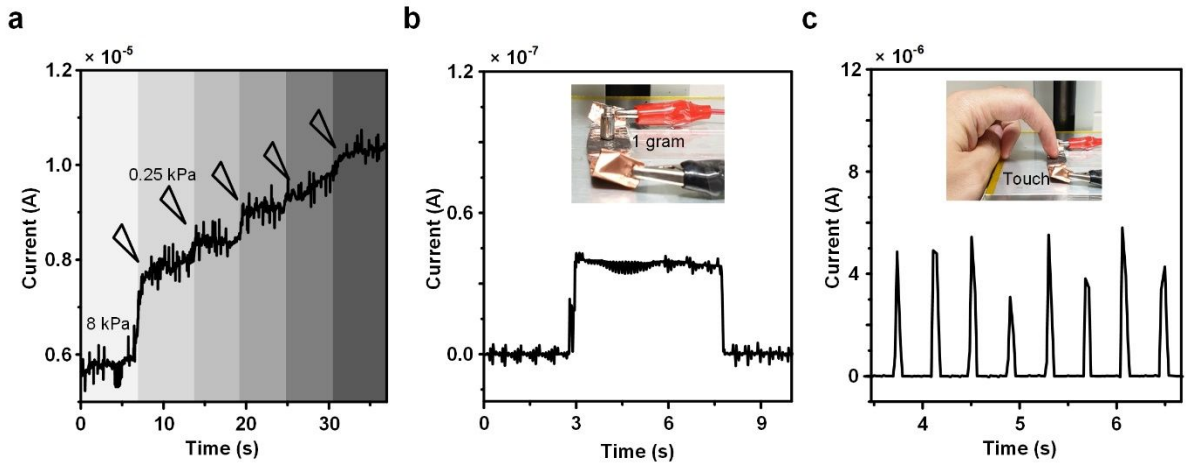

Figure S8. a) Current of the sensor with an increasing pressure of 250 Pa. Sensor responses b) to the loading of a tiny object (1 g) and c) to finger touch

a

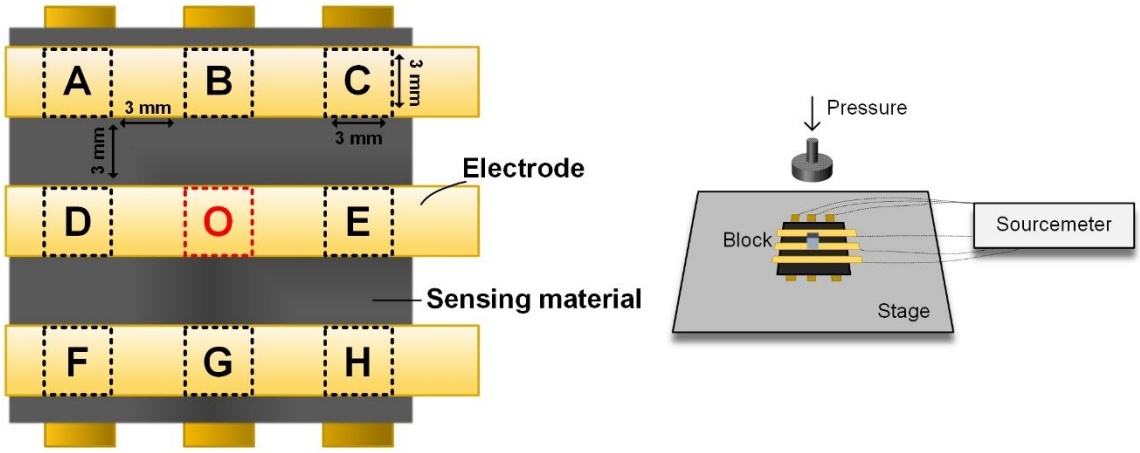

b

Mesh-based sensor (Planar state)		
0.01 μA	0.04 μA	0.01 μA
0.03 μA	**0.02 mA**	0.03 μA
0.002 μA	0.005 μA	0.002 μA

Conventional sensor (Planar state)		
3.57 μA	5.91 μA	5.18 μA
4.26 μA	**6.07 μA**	5.06 μA
2.08 μA	2.07 μA	2.24 μA

c

Mesh-based sensor (Bent state)		
0.001 μA	0.007 μA	0.04 μA
0.02 μA	**8 μA**	0.004 μA
0.01 μA	0.02 μA	0.004 μA

Conventional sensor (Bent state)		
3.67 μA	5.91 μA	0.16 μA
0.46 μA	**0.463 μA**	0.21 μA
0.16 μA	0.36 μA	0.19 μA

Figure S9. a) Schematic diagram of the electrode arrangement and setup for the crosstalk test. b,c) Current values of the nine cells of the mesh-based sensor and the conventional sensor under a pressure of 40 kPa applied on the center of the cell-O in planar and bent states

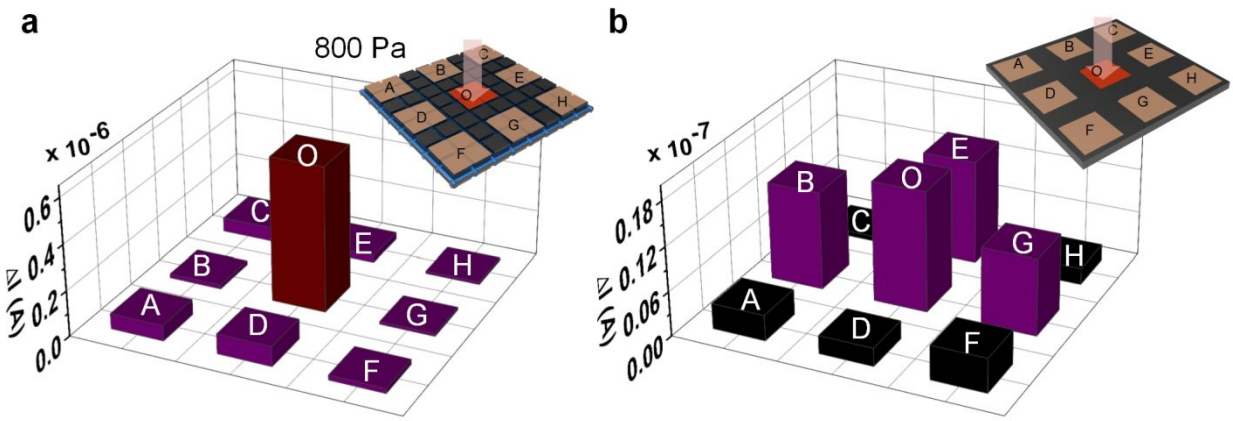

Figure S10. The changes in current of the 9 cells of the a) mesh-based sensor and the b) conventional sensor under a pressure of 800 Pa applied on the center of the cell-O

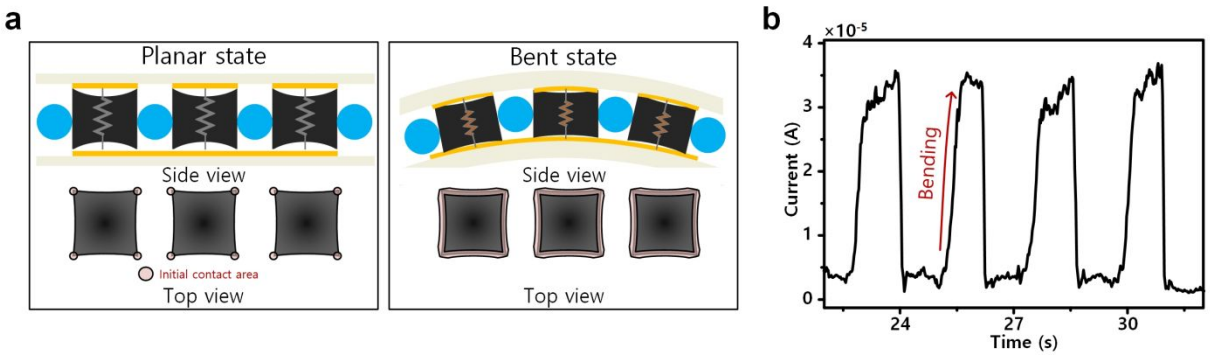

Figure S11. a) The initial contact area between the sensing material and electrode in planar and bent state. b) Transient response to the repeated cycles of bending.

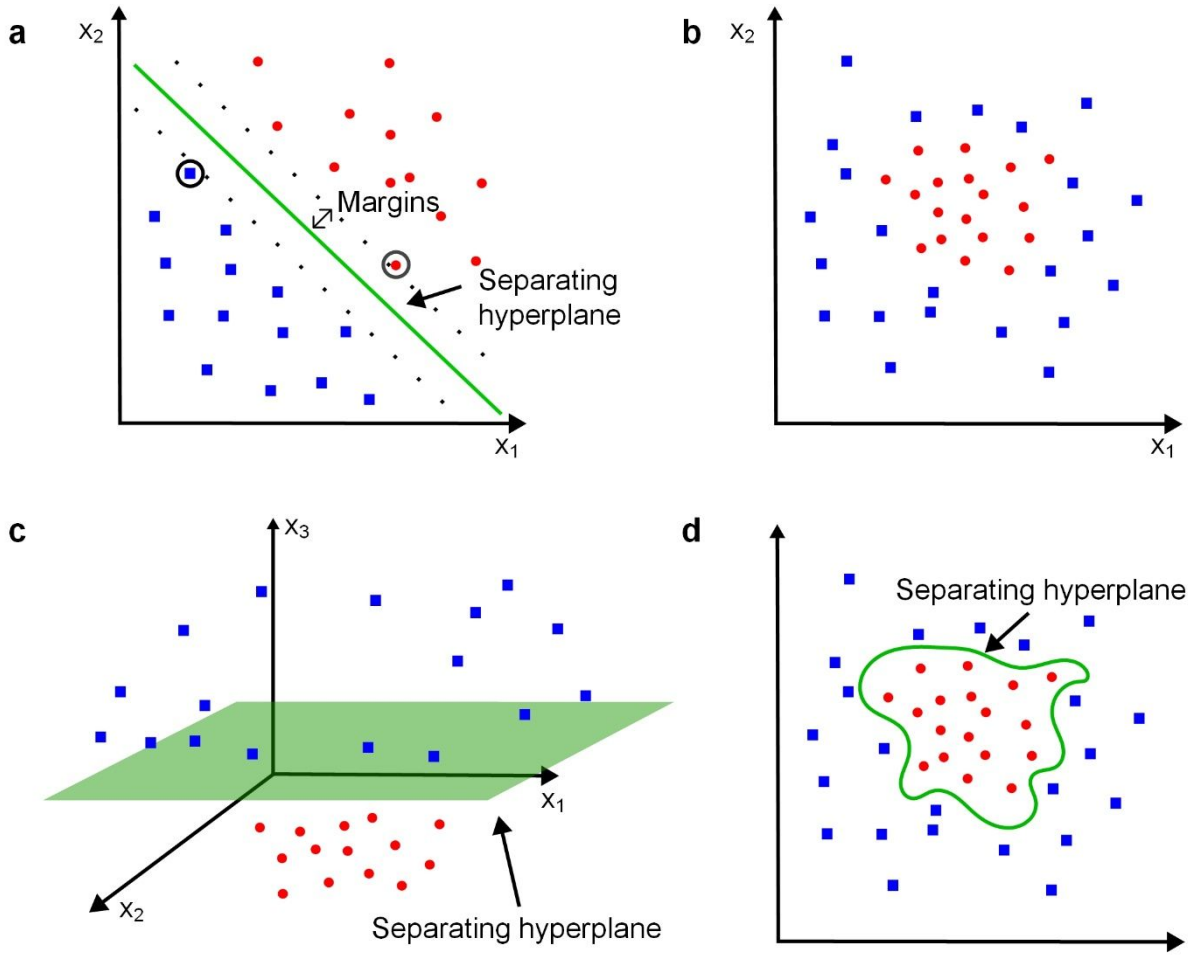

Figure S12. Various data point distributions and SVM classification examples. a) Separating hyperplane and margin in 2D, determined by support vectors (black circles). b) Linearly inseparable case in 2D. c) Linearly separated in 3D by adding an additional dimension with the same data of (b). d) Separated with using the nonlinear kernel in the same data of (b).

The objective of the SVM is to find a separating hyperplane in an N-dimensional space, where N is the feature dimension. The separating hyperplane is defined by maximizing a margin that is the distance between the hyperplane and a supporting vector, denoted with a blank circle in Figure S9a. Binary classification is the process of classifying a given set of elements into two

predefined groups. One group can be labeled y = 1, and the other group can be labeled y = -1. Given training data comprised of pairs $(\boldsymbol{x}_i, y_i)$, i $\in \{1,...,d\}$ where $\boldsymbol{x}_i \in R^n$ and $y_i \in \{1, -1\}$, the SVM requires the solution of the following optimization problem:

$$\min_{\boldsymbol{w},b,\xi} \frac{1}{2}\boldsymbol{w}^T\boldsymbol{w} + C\sum_{i=1}^{d}\xi_i \quad (1)$$

$$subject\ to\ \ y_i\left(\boldsymbol{w}^T\phi(\boldsymbol{x}_i) + b\right) \geq 1 - \xi_i\,,\ \xi_i \geq 0. \quad (2)$$

where $\boldsymbol{w}$ is a normal vector of the plane. $\phi(\cdot)$ is a mapping function related to a kernel trick. ξ and C are the slack variable and penalty parameter, respectively, related to whether the margin is hard or soft.

When the given training data are not linearly separable, they can be addressed using kernel tricks (Figure S9b). Dimensional or spatial alignment of data can be manipulated with the mapping function $\phi: R^n \rightarrow R^m$. As the primal and dual optimizations require the inner product of $\boldsymbol{w}$ itself, the kernel function can usually be defined as follows:

$$K(\boldsymbol{x}_i, \boldsymbol{x}_j) = \phi(\boldsymbol{x}_i)^T\phi(\boldsymbol{x}_j) \quad (3)$$

Specific kernel functions are required to acquire additional dimensions for inseparable data and convert them into a spatial distribution (Figure S9c). These data are linearly separated by hyperplanes. Otherwise, hyperplanes in mapped spaces that are not "planes" in the original space can be obtained through kernel tricks (Figure S9d). One of the most adopted kernel tricks is the radial basis function (RBF) kernel as follows:

$$K_{RBF}(\boldsymbol{x}, \boldsymbol{x}') = \exp\left(-\gamma\|\boldsymbol{x} - \boldsymbol{x}'\|^2\right) \quad (4)$$

where γ is a user-defined hyperparameter. This article also uses this kernel, as it contains the expression of Euclidean distance, which is crucial for the classification scheme in this article.

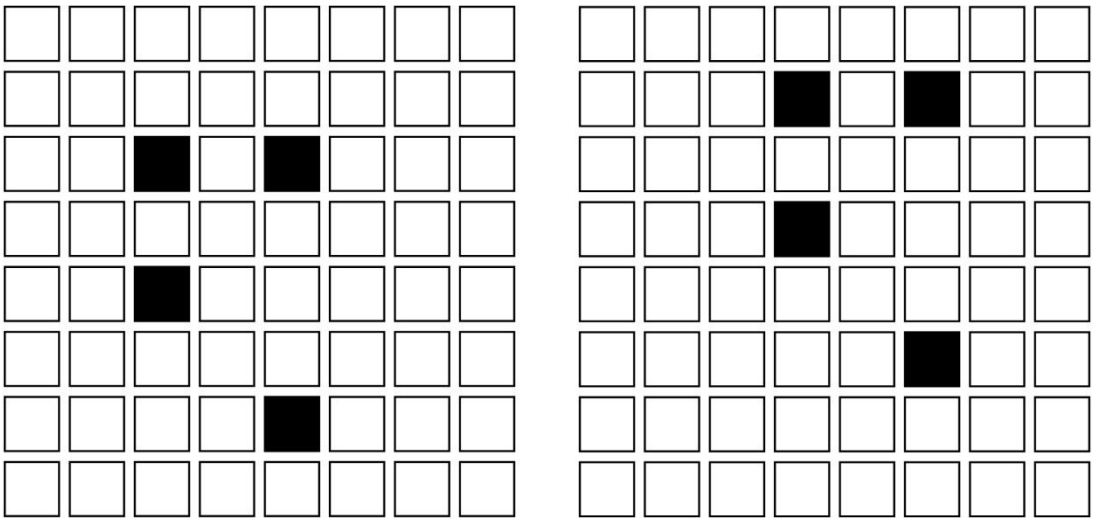

Figure S13. Two sample cases of Braille "N." The two samples pressing different positions show the same shape.

Figure S10 illustrates two different sensor reading results in two different flattened vectors. The Braille translation shifts the position of the entries of the vector, which is identical to a linear transformation by multiplying the power of the cyclic permutation matrix. This entry shift can be interpreted as rotational symmetry with respect to the sum of the standard basis of R^n. This is the rationale behind using the RBF kernel, as the rotation preserves the Euclidean distance of such vectors in R^n. Hence, this distance becomes the main criterion for generating the hyperplane in this nonlinear SVM problem. For a demonstration, ideal Braille reading data are generated. Each Braille letter has 100 vector data by multiplying 100 different perturbations $\sim N(1, 0.05)$, and comprises a synthesized dataset. The dataset is augmented with cyclic permutations of the vectors. As shown in Table 1, each letter has a prediction accuracy above 80%. This result shows that RBF-kernel SVM is suitable for Braille classification.

Letter	Accuracy	N	0.819
A	1	O	0.817
B	0.81	P	0.816
C	0.812	Q	0.818
D	0.811	R	0.815
E	0.809	S	0.823
F	0.808	T	0.812
G	0.814	U	0.819
H	0.819	V	0.816
I	0.811	W	0.818
J	0.811	X	0.825
K	0.825	Y	0.813
L	0.827	Z	0.813
M	0.814	**Mean**	**0.823**

Table S1. 10-fold cross-validation prediction accuracy with an average of 1000 procedures using ideal Braille data

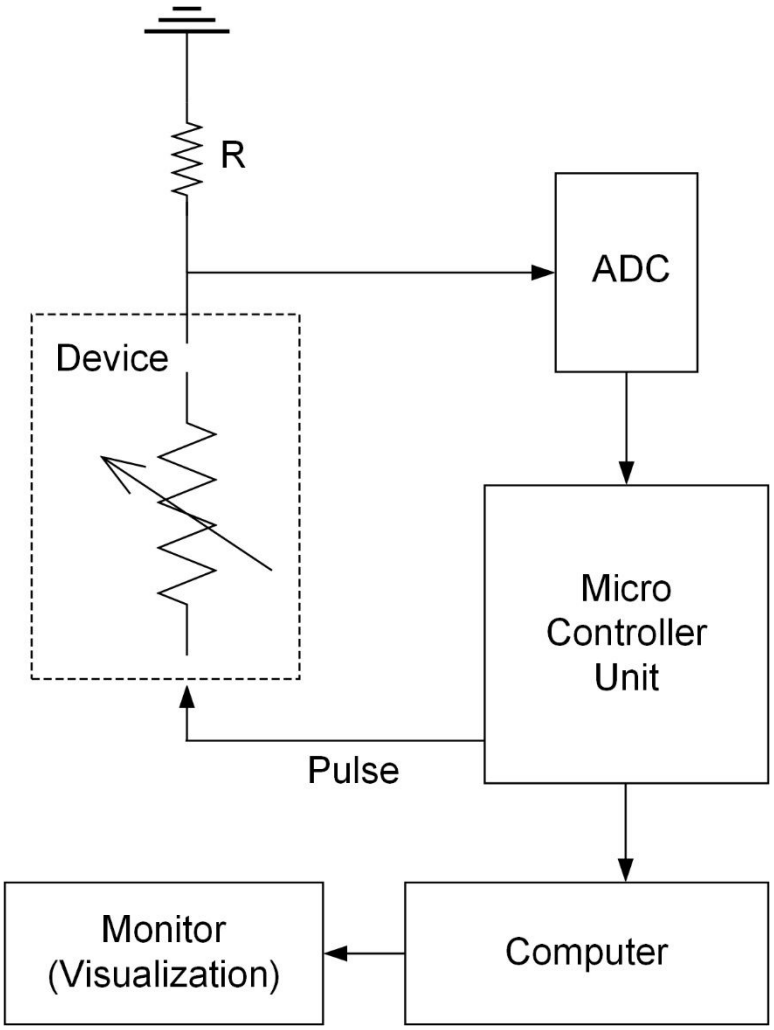

Figure S14. Block diagram of the current measurement, data acquisition, and visualization system